Performance characteristics and internal flow patterns in a reverse-running pump–turbine

R Barrio[1]*, **J Fernández**[2], **E Blanco**[1], **J Parrondo**[1], and **A Marcos**[2]
[1]Departamento de Energía, Universidad de Oviedo, Campus de Viesques, Gijón, Spain
[2]Departamento de IMEM, Universidad de Extremadura, Escuela de Ingenierías Industriales, Badajoz, Spain

The manuscript was received on 19 February 2011 and was accepted after revision for publication on 17 June 2011.

DOI: 10.1177/0954406211416304

Abstract: Vaneless centrifugal pumps are reversible turbomachines that can operate also as centripetal turbines in low and very low-head power plants. However, the general performance in reverse mode is difficult to predict since the internal flow patterns are different from pump mode and the performance characteristics are not usually provided by manufacturers. This article presents numerical and experimental investigations on the operation of a reverse-running pump–turbine. The numerical calculations were carried out by solving the full unsteady Reynolds-averaged Navier–Stokes equations with the commercial code Fluent for several flowrates between 20 per cent and 160 per cent of rated conditions and both modes of operation. A complementary series of experimental measurements were performed in a test rig in order to obtain the general characteristics of the machine in pump and turbine modes, with the purpose of validating the numerical predictions. Once validated, the numerical model was used to investigate the flow patterns at some significant locations by means of pressure and velocity contours, and also by vector maps. Additionally, the model allowed the estimation of the steady load on the impeller as a function of flowrate in both modes of operation. It was concluded that, while the radial load in reverse mode is three times smaller than in pump mode, the axial load can be up to 1.6 times larger.

Keywords: centrifugal pump, reverse operation, unsteady CFD simulations, internal flow patterns, steady load

1 INTRODUCTION

Centrifugal pumps are very common fluid machines used to supply energy to a circulating fluid (usually water) by means of a bladed rotor with axial inlet and radial outlet which is called the impeller. The outgoing flow from the impeller is collected by a stationary element called the volute, a sort of duct around the impeller periphery with increasing cross-section that guides the fluid towards the pump outlet port.

Centrifugal pumps with vaneless volute are fully reversible turbomachines, and thus they can work also as centripetal turbines extracting energy from a flow of water to supply power to a generator [**1**–**3**]. Although there is a penalty in the maximum efficiency attained when compared to normal operation, centrifugal pumps can compete with conventional Francis turbines in low and very low-head power plants because of their simple geometry, high availability, and easy and cheap maintenance [**4**, **5**]. All these facts reduce the capital cost of the plant, and also the cost of the energy generated, which is especially desirable in developing countries with a continuously increasing energy demand.

However, the internal flow in a reverse-running pump–turbine is different from the Francis turbine due to the lack of guide vanes; also, the general performance is difficult to predict since characteristics in reverse mode are not usually provided by pump

*Corresponding author: Universidad de Oviedo, Departamento de Energía. Campus de Viesques, 33203 Gijón, Asturias, Spain.
email: barrioraul@uniovi.es

manufacturers. Therefore, the operation of centrifugal pumps as centripetal turbines has been investigated for years [**6**], which have led to several studies reported in the scientific and technical literature. Most of these studies are purely experimental and focus on the reverse operation of a specific pump [**7**, **8**] or a series of pumps [**9**, **10**], and usually conclude with the proposal of semi-empirical correlations to predict the performance characteristics in reverse mode from those obtained in pump mode.

In addition, the continuous improvement of the computational fluid dynamics (CFD) techniques makes them an attractive tool to be used for the prediction of the general performance and flow properties of centrifugal turbomachinery. This may be achieved by the numerical resolution of the Reynolds-averaged Navier–Stokes equations for unsteady flow (URANS, unsteady Reynolds-averaged Navier–Stokes) with a proper code. Several numerical studies on vaneless-volute centrifugal pumps in reverse operation have been reported in the technical literature, like the ones by Tamm *et al.* [**11**], Natanasabapathi and Kshirsagar [**12**], Derakhshan and Nourbakhsh [**13**], Derakhshan *et al.* [**14**], or Fernández *et al.* [**15**]. These studies have proven that unsteady numerical simulations can provide a reasonable estimation of the general performance of the machine from an engineering point of view, showing typical errors with the experimental data below 10 per cent. Much less effort has been devoted, however, to investigate: (a) the variation of the internal flow patterns when operating in reverse mode and (b) how these patterns are affected by modifications in the machine's point of operation.

This article presents a numerical investigation on a reverse-running pump–turbine with the main purpose of predicting both the general performance and the detailed characteristics of the internal flow. The body of this article is organized into five sections.

1. Section 2 presents the geometry and general parameters of the test pump, some details of the numerical model and the grid generated, and also the conditions imposed in the numerical calculations.
2. Section 3 shows details on the test rig, procedure, and instrumentation used for the experimental measurements. Also, it presents a comparison between the numerical and experimental heads, power and efficiency curves and, in addition, between the static pressure distributions at the periphery of the impeller.
3. Once the model is validated, the flow patterns in both modes of operation are presented in Section 4 by means of contour and vector maps obtained at the inlet and outlet of the impeller and also at the near-tongue region.
4. Section 5 shows some results about the variation of the steady load on the impeller with the type of operation and the flowrate.
5. Finally, the main conclusions of this study are summarized in Section 6.

2 TEST PUMP AND NUMERICAL PROCEDURE

2.1 Pump geometry and numerical model

This investigation was carried out in a commercial centrifugal pump with a vaneless-volute casing. The pump impeller has an exit diameter of 200 mm and seven twisted backward blades of logarithmic profile. The performance values at rated conditions obtained experimentally are $\phi = 0.012$ and $\psi = 0.15$. The non-dimensional specific speed is $\omega_S = 0.45$. Additional data on the pump geometry can be seen in Table 1.

The numerical model of the test pump comprises four modules, each generated and meshed independently: (a) inlet duct, (b) impeller, (c) volute, and (d) diffuser and outlet duct (Fig. 1). The inlet and outlet ducts were included in the model to take apart boundary conditions. The mesh in the ducts and in the outlet diffuser was generated with prismatic cells due to the relatively simple geometry at these fluid regions. In contrast, the impeller and volute modules were meshed with tetrahedrons of 0.003 m edge in average size, due to their better adaptation to complex geometries, as observed in Fig. 1. The size of the mesh in each fluid region and the total number of cells are presented in Table 2. The cells were refined (with a typical length of 0.001 m) near strategic locations, such as the leading and trailing edges of the blades (see details of the impeller in Fig. 1) and the volute tongue. The magnitude of the equiangle skew was kept below 0.6 for 98 per cent of the cells in the mesh, which prevents an excessive cell distortion and improves the numerical calculations.

The simulations were performed with the commercial code Fluent [**16**]. This code was used to solve the full three-dimensional (3D) URANS equations with

Table 1 Main geometrical parameters of the test pump

Impeller eye diameter (m)	0.057
Impeller exit diameter (m)	0.200
Impeller exit width (m)	0.016
Number of blades	7
Blade exit angle (degrees)	29
Tongue-tip radius (m)	0.117
Impeller–tongue radial gap (%)	17

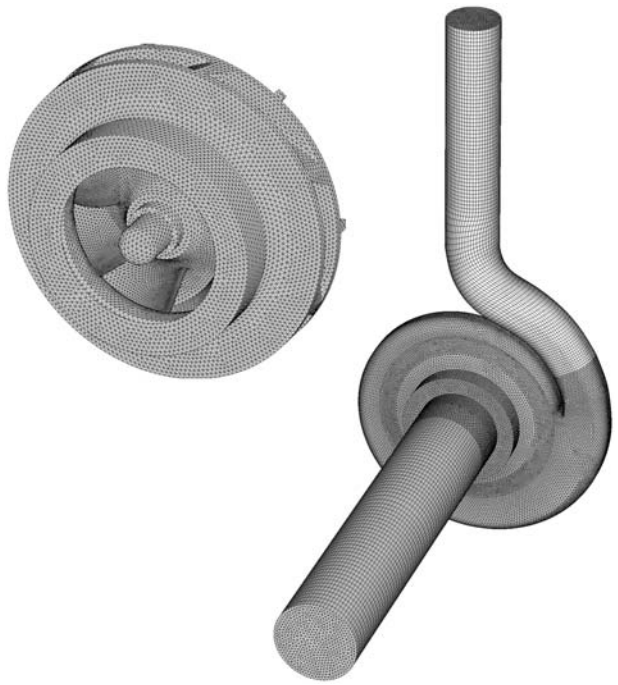

Fig. 1 General geometry and mesh generated with the details of the impeller

the finite volume method. The convection terms of the flow equations were approximated by second-order upwind discretizations, whereas central difference schemes were used for the diffusion terms. The time-dependent term scheme was a second-order implicit. The coupling between velocity and pressure was established by the SIMPLE algorithm. Turbulent effects were incorporated by means of the re-normalization group (RNG) k–ε model together with standard wall functions to calculate the flow variables near solid boundaries, supposed as adiabatic walls with a non-slip shear condition. The boundary conditions imposed in pump operation were a constant total pressure at the inlet and a constant static pressure proportional to the amount of kinetic energy at the outlet. The latter condition represents the particular case of a free discharge into a large reservoir through a valve. For operation in turbine mode, a constant total pressure at the inlet and a constant static pressure at the outlet were established. The specific magnitude of the boundary parameters was determined from the experimental measurements, as explained in following sections. These types of boundary conditions, imposed at some distance from the machine, result in a flow that is less distorted and more realistic than when defining, for instance a fixed flowrate. The relative motion between the impeller and the rest fluid modules was established by the definition of sliding mesh interfaces to exchange data of the cells at both sides.

Table 2 Number of cells in each fluid region

Inlet duct module	128 271
Impeller module	452 648
Volute module	241 079
Diffuser and outlet duct modules	98 137
Total	920 135

2.2 Numerical calculations and sensitivity analysis

Steady-state calculations were performed at first for a fixed angular position of the impeller (i.e. frozen-rotor interface) until achieving steady convergence. The resulting velocity and pressure fields were used subsequently to initialize the unsteady flow simulations. Each impeller revolution was computed in a time sequence of 224 time steps, which gives a time step size of 1.531×10^{-4} s for a speed of rotation of 1750 r/min. The convergence criterion established for each time step to accept the numerical results was to reduce the scaled residuals below 10^{-5}. At least five impeller revolutions were needed to achieve unsteady convergence, in the sense that the flow reached a stabilized periodic solution, as can be seen in Fig. 2.

The effect of the grid size on the numerical predictions was studied before carrying out the bulk of the calculations. Several meshes ranging from 4×10^5 to 2×10^6 cells were generated in order to investigate the relative change in some reference variables when increasing the density of the grid. The reference variables chosen were the flow coefficient ϕ and the head coefficient ψ in pump operation. These coefficients are defined as

$$\phi = \frac{Q}{\omega d^3} \tag{1}$$

$$\psi = \frac{gH}{\omega^2 d^2} \tag{2}$$

Figure 3 shows the magnitude predicted for each grid size, where ϕ and ψ are normalized by the values obtained with the finest mesh; as observed, there is little variation in the reference variables when increasing the size of the grid. The results of this grid-dependence analysis were used to estimate the numerical accuracy following the procedure of Celik *et al.* [**17**]. With the grid used in the final calculations, numerical uncertainties of 1.6 per cent and 0.43 per cent were estimated for the flow and head coefficients, respectively.

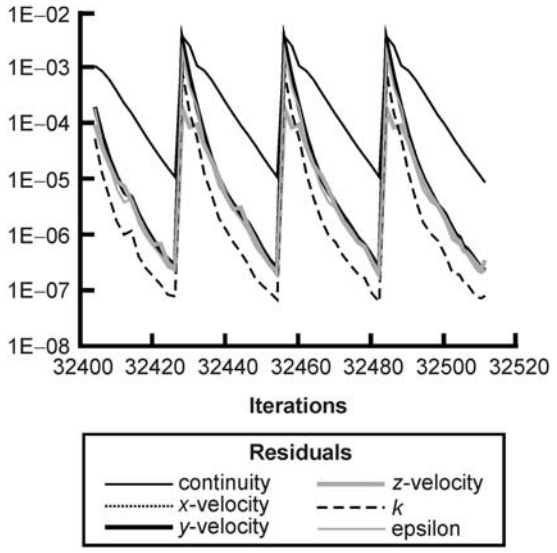

Fig. 2 Time convergence of the scaled residuals

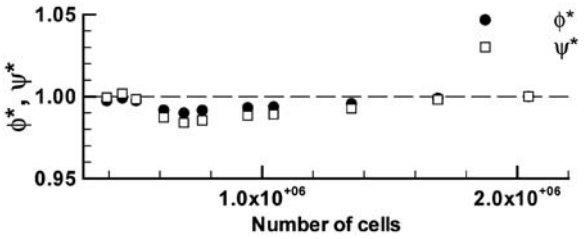

Fig. 3 Results of the grid-sensitivity analysis

The dependence of the numerical predictions with respect to the time step size was investigated additionally; for this purpose, the number of time steps per impeller revolution was modified as $t \cdot 2^n$, where t is the number of impeller blades and n ranges from 2 to 6. In this case, the differences obtained were even lower, showing relative magnitudes below 0.5 per cent. Finally, simulations with: (a) the standard, RNG, and realizable k–ε models, (b) standard and shear stress transport k–ω models, and (c) Reynolds stress model were performed to roughly check the influence of the turbulence model on the calculations. It was observed that the numerical predictions of ϕ and ψ were virtually unaffected by the turbulence model chosen. In conclusion, it can be said that the set of parameters imposed for the final calculations can be considered as a reasonable compromise between numerical accuracy and computational cost.

3 LABORATORY TESTS AND EXPERIMENTAL VALIDATION

3.1 Experimental facility and procedure

The numerical simulations were carried out for several flowrates ranging from 20 per cent to 160 per cent of rated conditions. Additionally, a series of experimental tests were conducted at laboratory to obtain the global performance characteristics of the machine when operating in both normal (pump) and reverse (turbine) modes. The experimental results were used subsequently to validate the predictions from the numerical model.

The laboratory facility consists of a tank of large capacity to which pumps can be connected through appropriate piping networks in a closed-loop (Fig. 4). The test pump (Fig. 4(a)) was driven by a direct current (DC) motor provided with a tachometer and a regulation device that allowed for adjustment of the rotational speed to a magnitude of 1750 r/min with a precision of ±1 r/min. The flowrate was finely regulated by a set of butterfly valves, located along the impulse pipeline; its magnitude was obtained with a precision of ±0.8 per cent by means of a KHRONE IFC010 electromagnetic flow meter. The pump was also instrumented with KISTLER 4043A10 piezoresistive pressure sensors and amplifiers to obtain the magnitude of the static pressure at the inlet and exit pipelines with an estimated combined precision of ±1.5 per cent. Additionally, several pressure taps located at a radial distance of 2.5 mm from the impeller exit were drilled at the front wall of the casing to obtain the static pressure distribution around the impeller periphery. A FAST-TECHNOLOGY series 2000 rotary torque sensor placed between the pump–turbine and the DC motor was used to calculate the torque with an estimated precision of ±0.8 per cent.

An auxiliary pump supplied the flowrate and head required by the test pump when operating in reverse mode (Fig. 4(b)). The former provides a flow of 160 m^3/h and a head of 90 m at the design point and is driven by an alternating current motor controlled by a frequency variator. This auxiliary pump generates a flow of water from the tank to the inlet of the test pump when the latter works as a turbine. The performance curves in this mode of operation were obtained also at a constant speed of 1750 r/min fixed by the electrical control equipment. The speed of the auxiliary pump was increased progressively to increase the flowrate and the head available; once the point of operation is fixed, flowrate, torque, and pressure measurements are made. The electric signals from the sensors were lead to an IMC – CRONOS PL/8 multichannel data acquisition module controlled by software from a desktop computer.

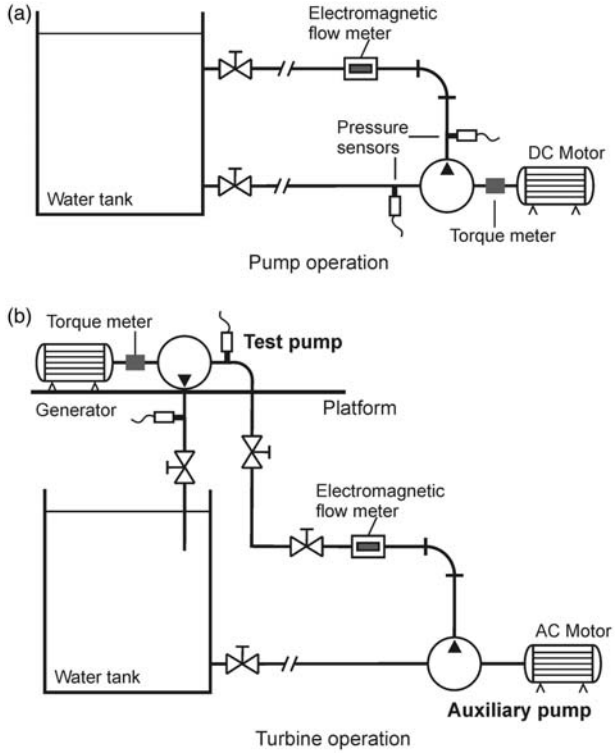

Fig. 4 Arrangement of the experimental rig in pump and turbine modes of operation

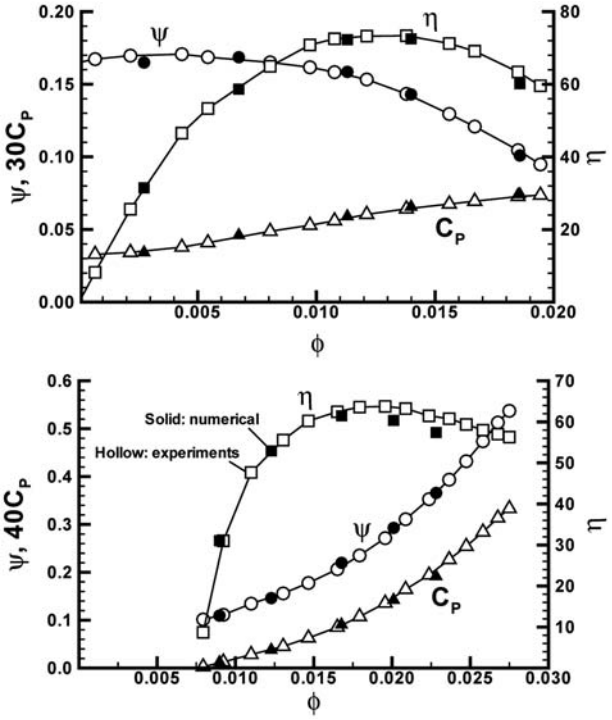

Fig. 5 General performance characteristics for operation in pump mode (top) and turbine mode (bottom)

The signals were stored in the computer and fast-Fourier transform processed to obtain the averaged magnitude of the measured variables. The resulting averaged magnitudes were used to calculate the performance curves of the machine in both modes of operation.

3.2 Comparison with numerical predictions

The total head (circles), power (triangles), and efficiency (squares) characteristics for operation in pump mode are presented in Fig. 5 (top) for a constant speed of 1750 r/min. The experimental measurements are shown by means of hollow icons, whereas the numerical predictions are plotted with solid icons. The relative uncertainty [**18**] in the best efficiency point resulted in ±1.5 per cent in head, ±0.8 per cent in power, and ±2.08 per cent in efficiency.

As observed, there is generally a good agreement between the experiments and the numerical predictions in pump mode. Both the experimental and numerical $\psi(\phi)$ curves show a negative slope with increasing flowrates, which is typical of centrifugal turbomachines [**1**]. Also, it is noted that the differences between the experiments and the numerical calculations are small, showing maximum relative errors of about 3 per cent for the lowest and the highest flowrates, and only of about 1.4 per cent for intermediate values. The comparison between the predicted and measured $C_P(\phi)$ characteristics shows an increasing power with flowrate, as expected for a centrifugal pump; in this case, typical differences in the range 1.5–3 per cent are obtained (the power coefficient C_P is scaled by a factor of 30 to fit the left vertical axis). Finally, the experimental and numerical $\eta(\phi)$ characteristics also show a good agreement: both curves show the same trend, and the maximum efficiency (slightly above 70 per cent) is obtained for a flow coefficient of about 0.012. In this case, the typical relative differences are below 3 per cent for low and intermediate values of the flowrate; only for the highest flowrate (160 per cent of rated), this difference increases up to 5 per cent.

The experimental and numerical heads, power, and efficiency characteristics for operation in turbine mode are presented also in Fig. 5 (bottom). The experimental uncertainty at rated conditions [**18**] resulted in ±1.52 per cent in head, ±0.8 per cent in power, and ±2.18 per cent in efficiency. As appreciated, there is a good agreement between the experiments and the numerical predictions for the $\psi(\phi)$ curve, which shows an increasing head with increasing flowrates, as expected for a centripetal turbine. The maximum relative differences obtained are below 3.5 per cent for all the test flowrates. Also, it is

observed that the numerical model captures the trend of the $C_P(\phi)$ curve properly, showing differences with the experimental data that are below 3 per cent for all the test flowrates (the power coefficient is scaled by a factor of 40 to fit the left vertical axis). Finally, it is seen that there is a good agreement between the experimental and numerical $\eta(\phi)$ characteristics, showing a maximum efficiency of about 61.5 per cent at $\phi = 0.017$, which is very close to the magnitude of 63 per cent obtained in the experimental measurements. A detailed comparison of the experiments and the numerical predictions shows average relative differences of about 3.5 per cent for moderate flowrates, which is a desirable range of operation due to the relative flat shape of the efficiency curve; only for the highest flowrate, this difference increases up to 5.5 per cent. According to these results, the non-dimensional specific speed of the pump in reverse mode results $\omega_{ST} = 0.3$.

The spatial distribution of the average static pressure around the periphery of the impeller is presented in Fig. 6 (top) for operation in pump mode and for three test flowrates. The variable φ is the angular coordinate, where $\varphi = 0^\circ$ in the figure corresponds to the tip of the tongue. The average static pressure is shown normalized by the dynamic pressure associated to the tangential velocity at the impeller periphery ($0.5\rho U^2$). As observed, there is quite a good agreement between the numerical predictions (lines) and the experiments (icons), especially for medium and high flowrates. The static pressure increases along the volute at 20 per cent flowrate due to the progressive reduction of the amount of kinetic energy as the cross-section of the volute is increased. In contrast, at 160 per cent flowrate, there is an excess of kinetic energy when compared to rated conditions, and thus the average static pressure decreases with the angular coordinate φ. At rated conditions, it is seen that the pressure distribution around the impeller is quite uniform due to the optimum coupling between the impeller and the volute, as expected for a centrifugal pump with volute casing [**1**, **3**]. The quantitative agreement between the experimental data and the numerical predictions can be considered as satisfactory, showing relative differences less than 5 per cent for most of the measurement locations. This difference increases up to 12 per cent at the tongue region only for the 20 per cent flowrate, which can be attributable to the abrupt pressure variation across the volute throat when operating at strong part load.

The angular distribution around the impeller of the average static pressure for operation in turbine mode is presented at the bottom of Fig. 6. As can be seen, the magnitude of the static pressure increases when

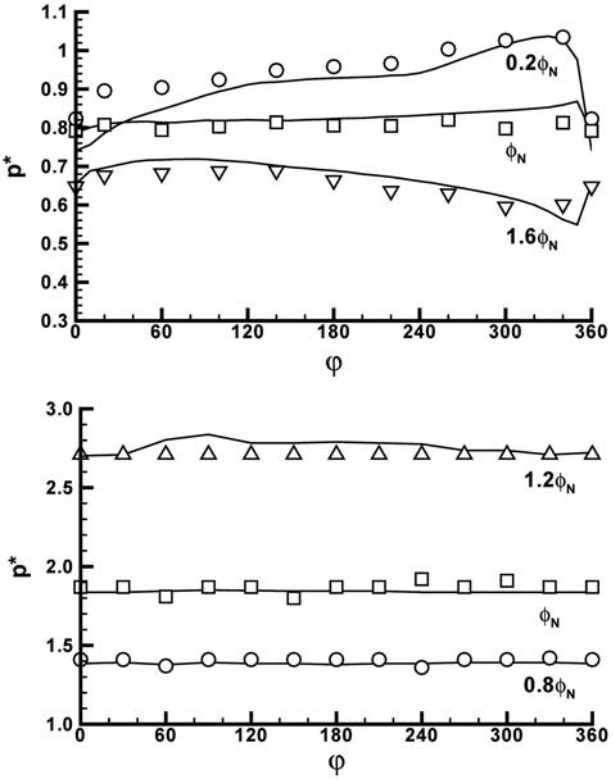

Fig. 6 Static pressure distribution around the impeller periphery for operation in pump mode (top) and turbine mode (bottom) and three test flowrates

the flow through the machine is increased. It is observed that the average pressure is about two times larger than in pump mode (as expected from the results shown in Fig. 5) and, additionally, that the pressure distribution around the impeller is more uniform, especially at low and medium flowrates. There is quite a good agreement between the experimental data and the numerical predictions, with relative differences that are typically below 3.5 per cent.

In conclusion, the good agreement between the experiments and the numerical predictions suggests that the numerical model can be used to investigate the performance of the machine and the general characteristics of the internal flow when operating in both normal and reverse modes. This will be undertaken in the following section.

4 GLOBAL AND LOCAL FLOW ANALYSES

4.1 Operation in pump mode

The flow distribution through a cross-sectional plane S located at the inlet of the machine (see sketch of Fig. 7) is presented in Fig. 8 for two test flowrates. This figure shows the contours of the normalized axial

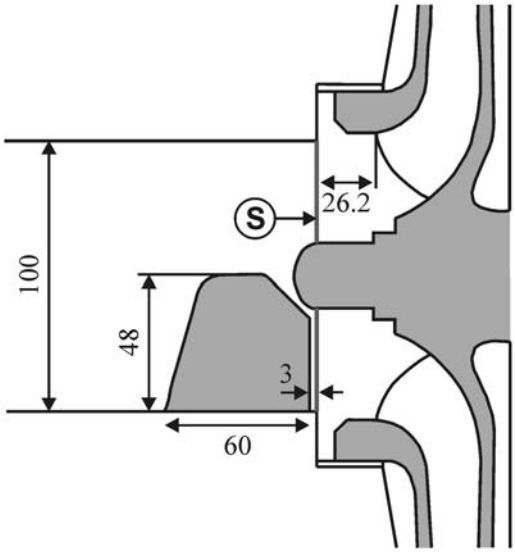

Fig. 7 Detail of pump's geometry at the inlet of the impeller, showing the inlet guide vane and the measurement section S

velocity defined as

$$V_{\mathrm{A}}^{*} = \frac{V_{\mathrm{A}}}{\omega\, r} \tag{3}$$

A negative magnitude of V_{A}^{*} means that the fluid flows from the inlet duct to the pump; in contrast, a positive magnitude of V_{A}^{*} implies that the fluid leaves the pump and flows towards the inlet pipeline. The projection of the absolute velocity vectors (i.e. tangential and radial components) on the cross-sectional plane is also shown in Fig. 8.

As seen, the flow distribution is significantly affected by the point of operation of the machine. This distribution is quite uniform through the whole inlet area for operation at rated conditions, showing a velocity field with a predominant component in the axial direction. A small region of low velocities can be observed at the bottom of the image, which is attributable to the wake behind an inlet guide vane located 3 mm from the inlet of the pump (Fig. 7). Also, a region with velocities in the range [−0.015 0] provoked by the boundary layer on the impeller nut is seen at the centre of the figure. The numerical results obtained are in accordance with the general design criteria for centrifugal pumps [**1**, **3**]. According to these criteria, the velocity triangle at the inlet of the impeller when operating at nominal conditions should be similar to the one presented at the bottom of Fig. 8. This triangle shows an absolute velocity V perpendicular to the direction associated with the tangential velocity U at the inlet of the impeller, which is consistent with the velocity field obtained at nominal conditions.

However, the obtained flow field is quite different for operation at strong part load, for example, at 20 per cent flowrate (top image). In this case, the magnitude of the component of V perpendicular to the direction of U must be smaller to reduce the flowrate. This develops a tangential component V_{U} that induces a fluid rotation in the same sense as the impeller, especially at the outer region of the inlet area. This effect is called prerotation and it is well reported in centrifugal pumps when operating at low flowrates [**3**, **19**]. Moreover, it is observed in the figure that the incoming flow of fluid is confined to the inner region of the inlet area, whereas an annulus of outgoing fluid can be seen at the outer region. This effect is called inlet recirculation, and it is observed also in centrifugal pumps below a certain capacity [**3**].

The contours of the normalized radial velocity, defined as

$$V_{\mathrm{R}}^{*} = \frac{V_{\mathrm{R}}}{\omega\, b} \tag{4}$$

for three test flowrates at the exit of the impeller are presented in Fig. 9 (b is the exit width of the impeller). The location of the trailing edge of the blades and the volute tongue is indicated in the figure. As observed, the radial velocity field at impeller exit depends on the operating point of the pump. In general, it is seen that this field is quite similar for operation at medium and high flowrates, with a region of high radial velocity near the pressure side (PS) of the blades and a zone of low radial velocity near the suction side (SS), thus showing the well-known jet-wake effect associated with the operation of centrifugal pumps [**19**, **20**]. Additionally, it can be noted that the radial velocity field for the highest flowrate is not uniform among the passageways: maximum radial velocities are obtained through the impeller channel that is located in front of the volute tongue.

In contrast, the velocity field obtained at 20 per cent flowrate is quite different from the former ones. The jet-wake effect associated with the passage of the impeller blades can be seen also at part load, showing maximum radial velocities near the PS of the blades, close to the hub of the impeller, and minimum magnitudes near the SS. However, regions of reverse circulation are observed now at the exit of the four passageways nearest to the volute tongue. The size of the recirculating region seems to increase as the blade approaches the tongue, being maximum when the passageway is located in front of it. This region takes up most of the passage exit area, and thus part of the flow is forced to exit the impeller close to the SS of the front blade of the channel.

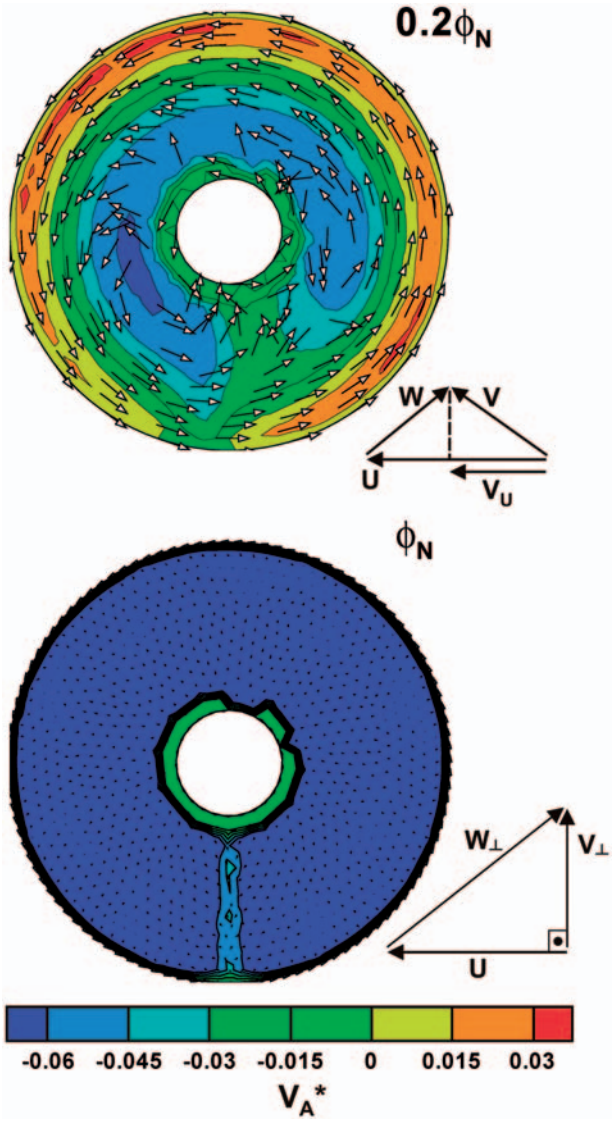

Fig. 8 Contours of axial velocity and velocity vectors at the inlet of the machine for operation in pump mode at 20 per cent and 100 per cent flowrate

This originates an additional jet of fluid between the wake of the blade and the recirculating region, which is especially evident for the passageway located at ∼20°–70°. As observed in Fig. 9, the net flow through the passageway is negative during part of the impeller cycle.

Figure 10 shows a contour map of the static pressure at the near-tongue region for the same flowrates of Fig. 9. The results of this figure were obtained in a cross-sectional plane located at impeller mid-span. The pressure is presented normalized by the dynamic pressure associated to the tangential velocity U at the periphery of the impeller. Also, this figure shows the velocity vectors within the impeller module in the relative frame of reference and, additionally, the absolute velocity vectors in the volute module. As seen, the static pressure increases along the impeller passageways from the inner to the outer sections, and the maximum pressure reached decreases as flowrate is increased, as expected for a centrifugal pump [**1**]. The relative flow in the impeller presents a good uniformity for medium and high flowrates, showing streamlines that follow the geometry of the blades. In contrast, it is observed that the relative flow within the passageways at 20 per cent flowrate presents regions of strong recirculation, as expected from the previous results of Fig. 9.

The interaction between the fluid exiting the impeller and the volute depends also on the point of operation of the pump. It is seen that the outgoing flow suitably matches the geometry of the volute at rated conditions: the flow progresses smoothly at both sides of the tongue and a stagnation point is clearly observed at its tip. However, the exit angle of the flow at 160 per cent flowrate is higher than that at rated conditions, and thus part of the fluid is forced to recirculate from the narrow side of the volute to the wide side by the push of the blades. This originates flow separation from the tip of the tongue, near the wide side of the volute, which can be observed in Fig. 10 as region with very low pressures. A similar but contrary effect is seen for the 20 per cent flowrate. In this case, part of the outgoing flow with a low exit angle is pushed by the blades and forced to circulate from the wide side of the volute to the narrow side. A region with a low pressure magnitude can be observed now at the tip of the tongue near the narrow side of the volute.

The results presented in this part of the article for operation below, equal to, and above rated conditions are in very good agreement with the general performance of centrifugal pumps reported in textbooks [**1**, **3**] and in the technical literature [**19**–**21**]. This supports that the numerical model can also be used to predict the performance of the pump when operating as a centripetal turbine, which will be shown in the following section.

4.2 Operation in turbine mode

A contour map of the static pressure and the velocity vectors in both the impeller (relative frame of reference) and the volute modules for three test flowrates are shown in Fig. 11. As expected for a centripetal turbine, the magnitude of the static pressure diminishes continuously from the outer to the inner section of the impeller due to the transmission of energy from the fluid to the blades. It is observed that the flow is well guided along the passageways at rated conditions, showing streamlines that follow

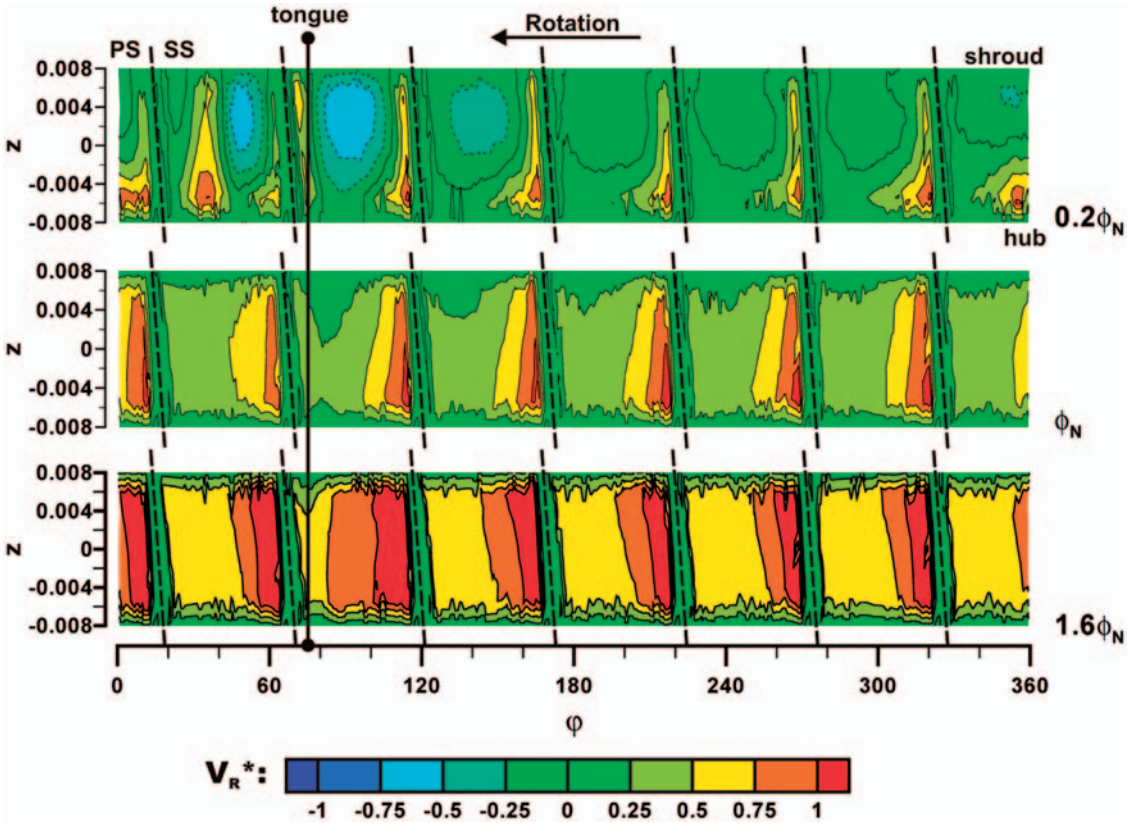

Fig. 9 Contours of radial velocity at the exit of the impeller for operation in pump mode and three test flowrates

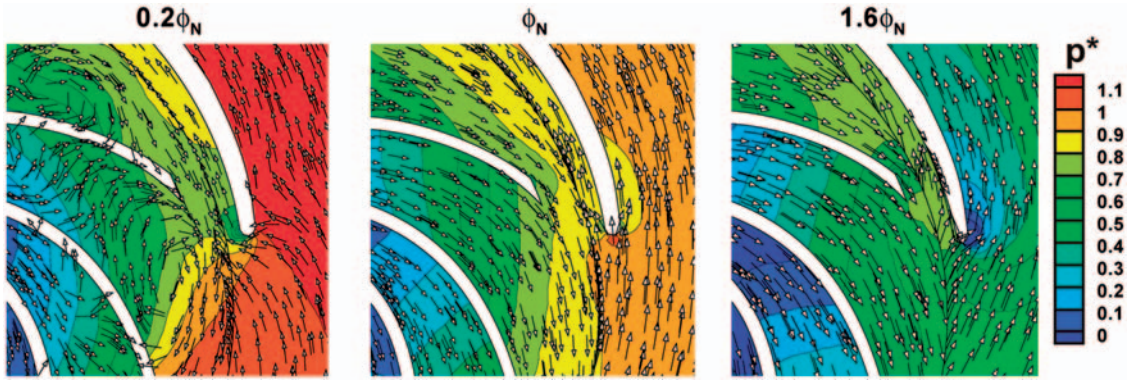

Fig. 10 Contours of static pressure and velocity vectors at the near-tongue region for operation in pump mode and three test flowrates

the geometry of the impeller blades. At low and high flowrates, however, the inlet angle of the flow deviates from that at nominal conditions, and thus the relative flow within the impeller channels does not match the blade geometry. This effect can be seen in Fig. 11 at 50 per cent flowrate, where a small zone of fluid recirculation is noted near the PS of the front blade of the channel. Also, a low-pressure core induced by a recirculating bulk of fluid is clearly observed near the SS of the rear blade at 140 per cent flowrate.

Figure 12 presents the magnitude of the normalized radial velocity around the inlet of the impeller for the same flowrates shown in the previous figure. It is clear that the inlet flow shows a good uniformity among the impeller channels at rated conditions, with a radial velocity magnitude that decreases

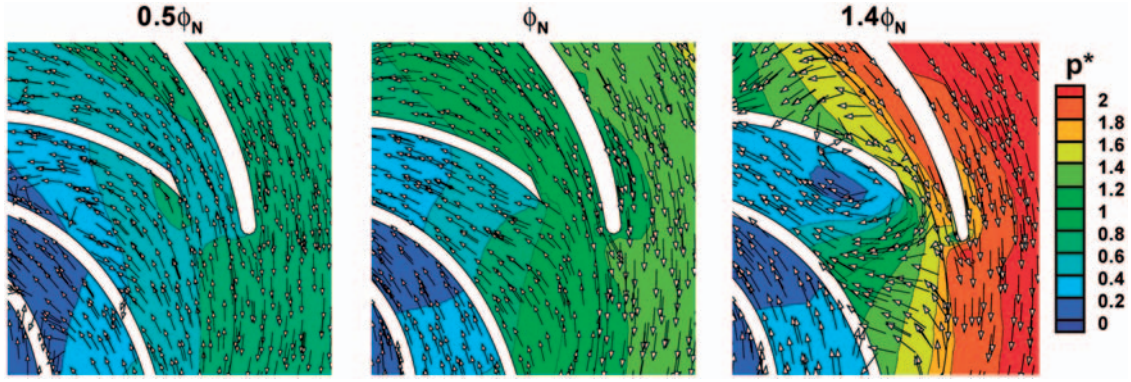

Fig. 11 Contours of static pressure and velocity vectors at the near-tongue region for operation in turbine mode and three test flowrates

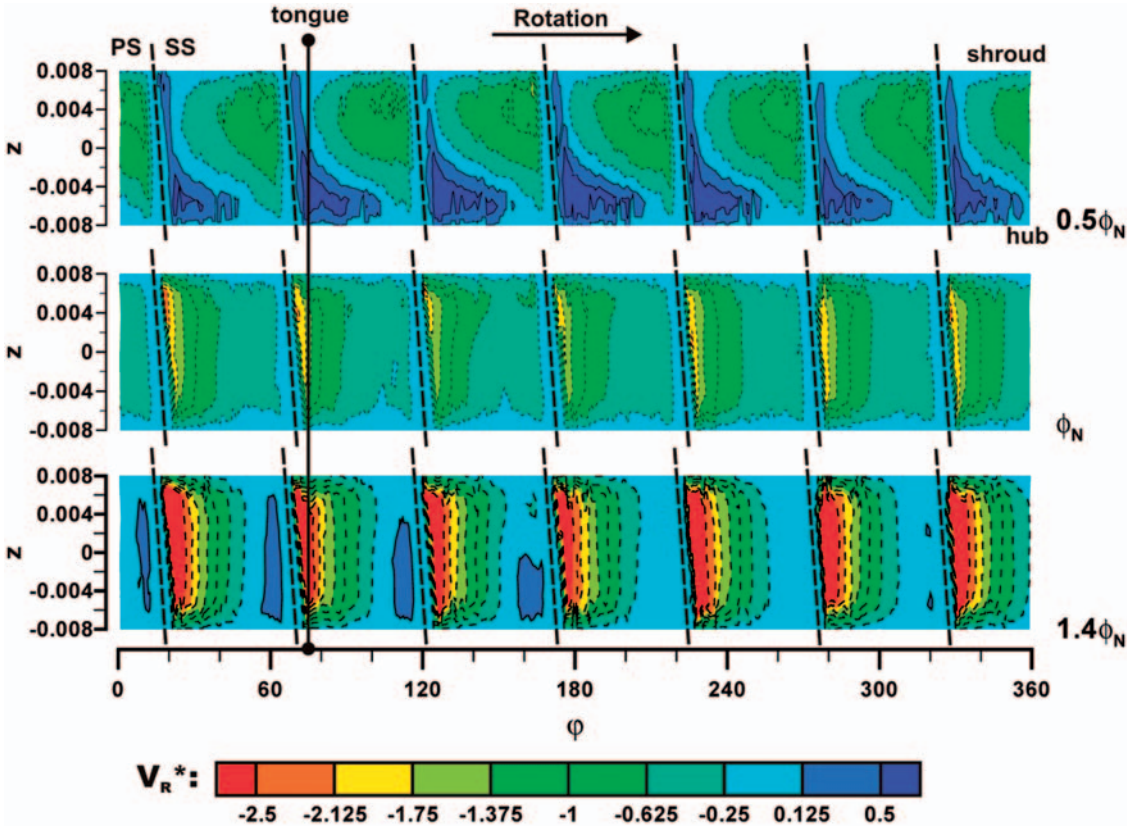

Fig. 12 Contours of radial velocity at the inlet of the impeller for operation in turbine mode and three test flowrates

continuously (in modulus) from the SS of one blade to the PS of the former blade. The same flow pattern (though higher radial velocities are obtained) can be observed as well at 140 per cent flowrate, but in this case, narrow regions of outgoing flow (i.e. a positive radial velocity) are noted near the PS of the four blades closer to the volute tongue. These regions are developed as a consequence of the large incidence angle of the incoming flow at high flowrates, which leads the fluid towards the SS of the blades and causes a small backflow near the PS. A similar effect is seen for the 50 per cent flowrate. The flow incidence angle

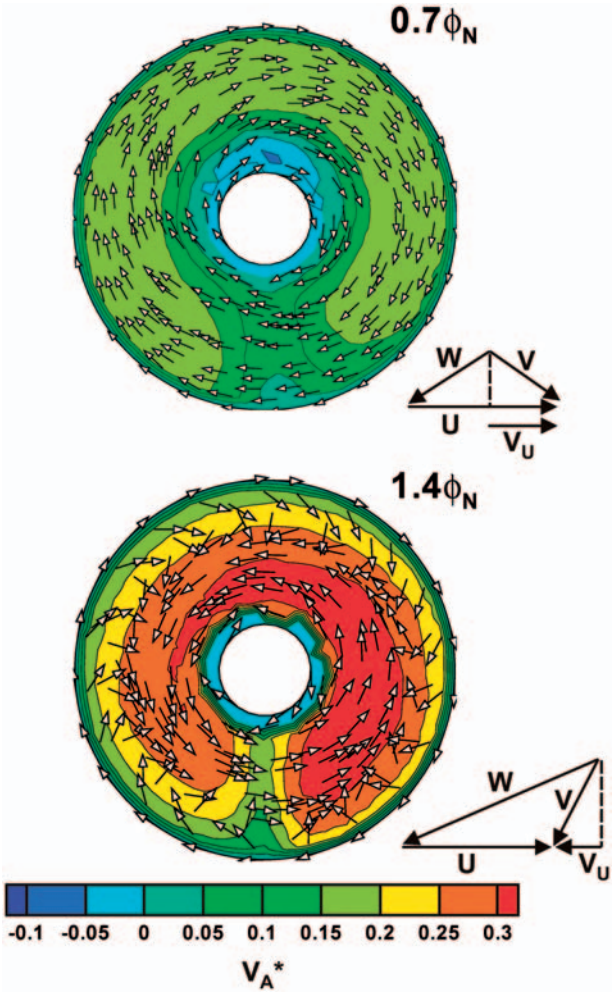

Fig. 13 Contours of axial velocity and velocity vectors at the outlet of the machine for operation in turbine mode at 70 per cent and 140 per cent flowrates

at low flowrates is small, and hence the fluid is led towards the PS of the blades, close to the shroud of the impeller, where maximum negative velocities are obtained. This flow deviation causes a significant backflow near the SS of all the impeller blades (especially close to the hub side), as observed in Fig. 12.

The flow pattern at the exit of the impeller for operation at part load and at a high flow rate is presented in Fig. 13. This figure shows the contours of the normalized axial velocity and also the projection of the absolute velocity vectors on the cross-sectional plane S (Fig. 7). As observed, the flow at impeller exit develops a whirl component whose rotation direction depends on the magnitude of the flowrate. Thus, it is seen in Fig. 13 that the outgoing fluid rotates in the same direction of the impeller at 70 per cent flowrate, in accordance with the velocity triangle at low flowrates indicated, whereas it rotates in the opposite direction at 140 per cent flowrate (see also the velocity triangle for high flowrates). This effect is called the post-rotation and it is usually reported in centripetal turbines when operating at low or high flowrates [**8**, **15**]. Additionally, the contours at 70 per cent flowrate show that the magnitude of the axial velocity increases in the radial direction. This is consistent with the results of Fig. 12, which showed that the fluid within the passageways flows close to the shroud of the impeller. In contrast, at 140 per cent flowrate, it is observed that the highest axial velocities are obtained at the inner regions of the exit area.

5 STEADY LOAD ON THE IMPELLER

The numerical model was used also to evaluate the steady load on the impeller as a function of flowrate when operating in both direct and reverse modes. This was done by storing the unsteady flow calculations during one full impeller revolution. The pressure and shear stress distributions on the impeller surfaces were integrated and time-averaged at each time step to obtain the magnitude of the steady load.

The amplitude and argument of the radial force defined as

$$F = \left(F_X^2 + F_Y^2\right)^{0.5} \tag{5}$$

for operation in pump (left) and turbine modes (right) are presented in Fig. 14 for all the test flowrates. The amplitude is shown normalized as

$$F^* = \frac{F}{0.5\,\rho\,U^2\,\pi\,d\,b} \tag{6}$$

As expected for a volute-type centrifugal pump operating in normal mode, the radial force shows minimum amplitudes near the nominal point of operation while increasing as the flowrate deviates from rated conditions [**1**, **3**]. Thus, it is seen that the average radial force can be up to five times larger when operating at 160 per cent flowrate, and up to nine times larger at 20 per cent flowrate. Additionally, it is observed that the argument of the radial force shows values located at the first quadrant for low and medium flowrates, whereas this argument is shifted towards the fourth quadrant for high flowrates. This follows the typical trend of the radial load observed in single-volute pumps [**22**].

A similar trend can be observed also for operation in reverse mode (right image), showing a minimum magnitude of the radial load at rated conditions and increasing amplitudes for both low and high flowrates. However, the maximum amplitudes obtained in reverse operation (when compared to rated conditions) are not as large as those obtained in pump operation. Hence, it is noted that the force amplitude

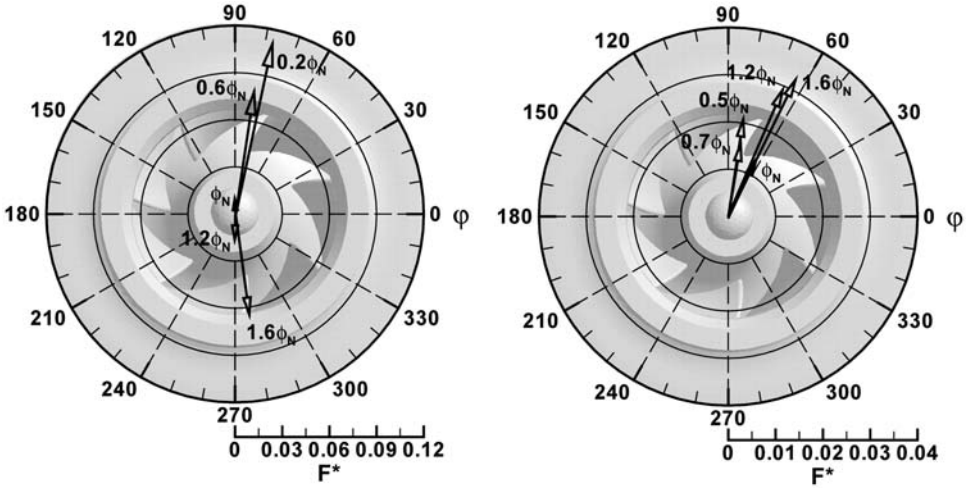

Fig. 14 Steady radial load on the impeller for operation in pump (left) and turbine mode (right) for all test flowrates

increases only about 1.2 times at 50 per cent flowrate and about 2.4 at 160 per cent flowrate, where the maximum amplitude is obtained. The results presented also show that the argument of the radial force remains between 60° and 90° for the whole range of operation investigated. Other significant result of Fig. 14 concerns the comparison between normal and reverse operations. It is seen that, while the amplitude of the radial force at rated conditions is similar for both modes of operation, the maximum magnitude predicted for this force is about three times smaller in reverse mode than in normal mode, as could have been expected from the better pressure uniformity around the impeller obtained in reverse mode (Fig. 6).

The normalized amplitude of the axial thrust defined as

$$F_Z^* = \frac{F_Z}{0.5\,\rho\,U^2\,\pi\,d^2} \tag{7}$$

as a function of flowrate can be seen in Fig. 15 for both modes of operation. It is observed in this figure that the pump operation presents an axial thrust that lies within the interval [0.02 0.04], showing a minimum amplitude near rated conditions, ϕ_N, and a maximum magnitude at the highest flowrate (about 1.5 larger than at the nominal point). The negative sign means that the direction of the thrust is opposite to that of the Z-axis, as indicated in the figure. A similar trend is observed in turbine mode: the axial thrust shows a minimum magnitude near the nominal point of operation (even lower than in pump mode) and, in this case, it presents a maximum amplitude (in modulus) at the lowest flowrate (almost six times larger than at rated conditions). Also, it is seen in Fig. 15 that the axial thrust changes from a negative to a positive

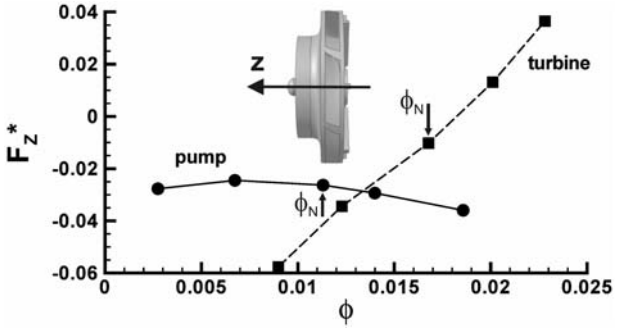

Fig. 15 Steady axial load on the impeller for both modes of operation and all test flowrates

direction when increasing the flowrate. The maximum amplitude of the axial thrust obtained in reverse mode is about 1.6 larger than that obtained in pump mode. All these results suggest that, while the radial load on the impeller seems to be less sensitive to a change in its sense of rotation, the magnitude of the axial thrust is significantly affected by both the sense of rotation and the machine's point of operation, showing amplitudes that can be up to six times larger than at rated conditions and up to 1.6 larger than in normal mode.

6 CONCLUSIONS

This article presented an investigation on the performance of a conventional centrifugal pump operating in normal and reverse modes. The investigation included calculations with the software Fluent in a

numerical model of the test pump, and also experimental measurements in a laboratory facility to obtain the general performance characteristics. The global conclusion of this study is that the performance of the reverse-running pump–turbine can be predicted by means of full 3D unsteady flow calculations with a proper CFD code: the comparison between the calculations and the experimental measurements showed typical differences in the range 3–5 per cent, which can be considered as reasonable from an engineering point of view. Significant differences above 10 per cent were observed only at the near-tongue region for operation in pump mode at very low flowrates (20 per cent of rated), which can be attributable to the flow complex interaction at this region that would require an enhanced treatment of the near-wall modelling.

The numerical results were used to investigate the flow patterns at several strategic locations in the machine; also, an estimation of the steady load on the impeller as a function of flowrate for both modes of operation was presented. The main conclusions about the flow are:

1. In pump mode, prerotation with recirculation was found at the inlet of the machine at strong part load (20 per cent flowrate). Also, internal recirculation and reverse flow at the exit of the impeller, close to the shroud side, were observed in the four passageways nearest to the volute tongue for the same flowrate. The jet-wake effect associated with the operation of centrifugal pumps was evident for all the test flowrates.
2. In turbine mode, internal recirculation in the impeller was found for low and high flowrates. The patterns of the flow at the inlet of the impeller showed large regions of backflow in all the impeller passageways (close to the SS of the blades, near the hub region) at 50 per cent flowrate. Backflow zones (of smaller magnitude) were observed also at 140 per cent flowrate near the PS of the blades; at this flowrate, the backflow regions are seen only in the four passageways nearest to the tongue. In addition, post-rotation at impeller exit was observed; the rotation of the fluid can be either in the same sense as the impeller (low flowrates) or in the opposite sense (high flowrates).

The main conclusions in regard to the steady load on the impeller are:

1. The magnitude of the steady load is significantly affected by the machine's point of operation. Thus, the steady load is minimum at rated conditions and increases for both lower and higher flowrates. The increment can be up to nine times larger in pump mode and up to six times larger in turbine mode.
2. Due to the better uniformity of the static pressure around the impeller, the maximum amplitude of the radial load in turbine mode is three times smaller than that in pump mode. In contrast, the magnitude of the axial load in reverse mode can be up to 1.6 times larger than that in pump mode, which is of significant importance to select the appropriate bearings if a pump is expected to work also as a centripetal turbine.

FUNDING

This work was supported by Ministerio de Educación y Ciencia (Spain) [grant number DPI2009-14455-C02-01].

REFERENCES

1 **Stepanoff, A. J.** *Centrifugal and axial flow pumps*, 1957, pp. 291–318 (John Wiley, New York).
2 **Kittredge, C. P.** Centrifugal pumps used as hydraulic turbines. *J. Eng. Power*, 1961, **A**, 74–77.
3 **Gülich, J. F.** *Centrifugal pumps*, 2008, pp. 689–710 (Springer-Verlag, New York).
4 **Williams, A. A.** Pumps as turbines for low cost micro hydro power. *Renewable Energy*, 1996, **9**, 1227–1234.
5 **Williams, A. A.** *Pumps as turbines: a user's guide*, edition 2, 2003 (ITDG Publishing, London).
6 **Nautiyal, H., Varun,** and **Kumar, A.** Reverse running pumps analytical, experimental and computational study: a review. *Renewable Sustainable Energy Rev.*, 2010, **14**, 2059–2067.
7 **Sinhama, H., Fukutomi, J., Nakase, Y., Chin, Y., Kuwauchi, T.,** and **Miyauchi, S.** Study of reverse running pump turbine. In Proceedings of 3rd ASME/JSME Joint Fluids Engineering Conference, San Francisco, California, 18–23 July 1999, paper 7340.
8 **Fernández, J., Blanco, E., Parrondo, J., Stickland, M. T.,** and **Scanlon, T. J.** Performance of a centrifugal pump running in reverse mode. *J. Power Energy*, 2004, **218**, 265–271.
9 **Williams, A. A.** The turbine performance of centrifugal pumps: a comparison of prediction methods. *J. Power Energy*, 1994, **208**, 59–66.
10 **Derakhshan, S.** and **Nourbakhsh, A.** Experimental study of characteristic curves of centrifugal pumps working as turbines in different specific speeds. *Exp. Thermal Fluid Sci.*, 2008, **32**, 800–807.
11 **Tamm, A., Braten, A., Stoffel, B.,** and **Ludwing, G.** Analysis of a standard pump in reverse operation using CFD. In Proceedings of 20th IAHR Symposium on *Hydraulic machinery and systems*, Charlotte, North Carolina, August 2000, paper PD – 05.

12 **Natanasabapathi, S. R.** and **Kshirsagar, J. T.** Pump as turbine – an experience with CFX – 5.6. In Proceedings of International ANSYS Conference, 2004, available from: www.ansys.com/events/proceedings/2004/PAPERS/127.PDF.

13 **Derakhshan, S.** and **Nourbakhsh, A.** Theoretical, numerical and experimental investigation of centrifugal pumps in reverse operation. *Exp. Thermal Fluid Sci.*, 2008, **32**, 1620–1627.

14 **Derakhshan, S., Mohammadi, B.,** and **Nourbakhsh, A.** Efficiency improvements of centrifugal reverse pumps. *J. Fluids Eng.*, 2009, **131**, 021103.

15 **Fernández, J., Barrio, R., Blanco, E., Parrondo, J. L.,** and **Marcos, A.** Numerical investigation of a centrifugal pump running in reverse mode. *J. Power Energy*, 2010, **224**, 373–381.

16 **Fluent Inc.** User's guide. 10 Cavendish Court, Lebanon, NH03766, 2006.

17 **Celik, I. B., Ghia, U., Roache, P. J., Freitas, C. J., Coleman, H.,** and **Raad, P. E.** Procedure for estimation and reporting of uncertainty due to discretization in CFD applications. *J. Fluids Eng.*, 2008, **130**, 01–1–01-4.

18 **Kline, S. J.** The purposes of uncertainty analysis. *J. Fluids Eng.*, 1985, **107**, 153–160.

19 **Brennen, C. E.** *Hydrodynamics of pumps*, 1994 (Oxford University Press, New York).

20 **Guelich, J. F.** and **Bolleter, U.** Pressure pulsations in centrifugal pumps. *J. Vibr. Acoust.*, 1992, **114**, 272–279.

21 **Miner, S. M., Beaudoin, R. J.,** and **Flack, R. D.** Laser velocimeter measurements in a centrifugal flow pump. *J. Turbomach.*, 1989, **111**, 205–212.

22 **Kittredge, C. P.** and **Cooper, P.** Centrifugal pumps: general performance characteristics. In *Pump handbook* (Eds I. J. Karassik, J. P. Messina, P. Cooper, and C. C. Heald), edition 3, 2001 (McGraw-Hill, New York).

APPENDIX

Notations

b	width (m)
C_P	$P \cdot (\rho\omega^3 d^5)^{-1}$, power coefficient (non-dimensional)
d	diameter (m)
F	force (N)
g	gravity (m/s^2)
H	head (m)
n	exponent
p	static pressure (Pa)
P	power (W)
Q	flowrate (m^3/s)
r	radius (m)
t	number of blades
U	tangential velocity (m/s)
V	absolute velocity (m/s)
W	relative velocity (m/s)

Greek symbols

ρ	density (kg/m^3)
ϕ	$Q(\omega d^3)^{-1}$, flow coefficient (non-dimensional)
φ	angular coordinate (degrees)
ψ	$gH(\omega^2\ d^2)^{-1}$, head coefficient (non-dimensional)
ω	rotation velocity (rad/s)
ω_S	$\omega Q^{0.5}\ (gH)^{-0.75}$, specific speed in pump mode (non-dimensional)
ω_{ST}	$\omega(P/\rho)^{0.5}\ (gH)^{-1.25}$, specific speed in turbine mode (non-dimensional)

Subscripts

A	axial
N	nominal
R	radial
U	tangential
X, Y, Z	components in principal directions

Superscripts

*	normalized magnitude